33RD CONGRESS
OF THE INTERNATIONAL COUNCIL
OF THE AERONAUTICAL SCIENCES
STOCKHOLM, SWEDEN, 4-9 SEPTEMBER, 2022

ICAS 2022 SWEDEN

EFFECTS OF ANISOTROPIC THERMAL CONDUCTIVITY OF COMPOSITE SHIELD ON THE ELECTROTHERMAL ANTI-ICING SYSTEMS

Xiaofeng Guo[1], Qian Yang[1], Haoran Zheng[1] & Wei Dong[1]

[1]School of Mechanical Engineering, Shanghai Jiao Tong University

Abstract

The performance of an electrothermal anti-icing system based on resistance heating elements embedded in CFRP(carbon fibre reinforced polymer) composite is of interest to aerospace. This paper analyzes the steady anti-icing process conjugating the thermal properties of CFRP composite. A coordinate transformation approach that resolves the principal axis in the local coordinate system to the global coordinate system is developed to exert anisotropic thermal conductivity in the irregular shape of the airfoil. Coupling with the anti-icing model, we estimated and compared the performance of a different combination of multi-layer structures based on the CFRP composite. For actual CFRP composite used in wing manufacturing, the anisotropic conductivity slightly affects the temperature distribution on the protected surface. It significantly affects the temperature distribution in the multi-layer structure. A temperature gradient that hurts the stability of composite would form along the airfoil surface direction in the structure.

Keywords: Anisotropic composite, Electrothermal anti-icing system, Numerical simulation, Conjugate heat transfer

1. Introduction)

Ice accretion will occur on airplane surfaces facing the wind due to the impingement of supercooled water droplets or the vapor condensation, destroying the aerodynamic performance and even threatening flight safety. An ice protection system is essential for the airplane to avoid the harm of ice accretion. The most widely used ice protection is the hot-air bleeding system on the wing leading edges and engine nacelles. Due to the urgency of lightweight and low energy consumption, CFRP(carbon fibre reinforced polymer) composite with excellent mechanical performance, such as high specific stiffness and strength, was applied extensively in the production of airplanes. The proportion of composite in the materials of Boeing787 is up to 50%. For composite components, the hot-air bleed ice protection is not applicable. Because bad thermal conduction performance of resin composite is harmful to the heat conduction from inner skin to the outer ice protection surface and high-temperature hot air from the engine could lead to thermal damage on composite components.
Owing to its flexibility and high efficiency, an electrothermal ice protection system that uses the joule heat of the resistance heater element installed beneath the composite skin is a good alternative. Boeing 787 is the first commercial aircraft to use electrothermal ice protection. Molten metal was sprayed on glass fiber fabric to form a conductive layer that was embedded in another laminate stack[1]. The thermal performance of the composite is unique. It is necessary to study the character of electrothermal anti-icing systems based on composite.
Research about electrothermal anti-icing systems is conducted early. NASA developed LEWICE, a computer code to simulate the electrothermal de-icing and anti-icing system. Then electrothermal ice protection experiments were conducted for validation. Silva[2, 3, 4, 5] developed a boundary-layer analysis method to calculate convection heat transfer around airfoil and runback water flow, which

is validated by experiments conducted by NASA [6]. Based on some assumptions, the steady electrothermal anti-icing process is analyzed based on the known heat power density distribution, whose results agree with the experiment data[7]. A tight-coupling method for the steady electrothermal anti-icing system was developed to calculate the convective heat transfer efficiency affected by surface temperature[8].

Thermal properties of skin material could affect the performance of the anti-icing system, such as the temperature distribution. Due to the existence of resin in carbon fiber reinforced polymer, a large temperature gradient that has an adverse effect on multi-layer composite structure will be formed. The effect of anisotropic heat conduction of shield layer on electrothermal anti-icing system is estimated based on coordinate transformation for anisotropic conduction and runback water model on the anti-icing surface. However, the thermal conductivity is artificially given [9].

The present work simulates the steady heat and mass transfer during the electrothermal anti-icing process on CFRP composite skin that provides Joule heating by the heating element installed beneath the composite structure. Heat and mass balance based on the modified Messinger model[10] in the liquid film is considered to get accurate results of the anti-icing process. A coordinate transformation method that is used to load the anisotropy for the irregular shape structure made of CFRP composite is developed to estimate the effects of low and anisotropic thermal conductivity on anti-icing performance at different compositions of the multi-layer structure under the same icing condition.

2. Thermal property of CFRP Composite

CFRP composite consists of carbon fiber and epoxy, in which carbon fiber is the enhanced phase while the epoxy is the matrix. The thermal conductivity of carbon fiber is orthotropic, including longitudinal and transverse conductivity. The orientation of fiber results in the anisotropic thermal conductivity of CFRP. The thermal property of CFRP is influenced mostly by the content of weaves in the fabric and fiber volume fraction, V_f, but influenced slightly by the temperature[11]. The longitudinal conductivity of fiber is almost ten times the transverse conductivity. The conductivity of matrix material and reinforced body should be considered for the effective conductivity of CFRP composite. The effective conductivity can be calculated by different models. For unidirectional lamina, the effective conductivity that is parallel to the fiber orientation can be calculated by the parallel model given as follows. The thermal conductivity of fiber and epoxy is shown in Tab.1. The fiber orientation is one of the principal axes of heat conduction. According to Ref.[12], if the principle heat conduction axes, x'-axis, has an included angle, θ with global x-axis, the in-plane global thermal conductivity of a ply, k_{x_s}, k_{y_s} can be calculated by the following equations,

$$k_{x_s} = k_{x'}|cos\theta| + k_{y'}|sin\theta| \tag{1}$$

$$k_{y_s} = k_{x'}|sin\theta| + k_{y'}|cos\theta| \tag{2}$$

where x', y' is the principal heat conduction axis in a single layer. And k_{z_s} is the out-of-plane thermal conductivity is equal to $k_{y'}$,

$$k_{z_s} = k_{y'} \tag{3}$$

In this paper, the composite laminate is formed with ten plies of the unidirectional lamina. The anisotropic thermal conductivity of the laminate can be obtained by the thermal resistance model.

$$k_x = \frac{1}{N}(\Sigma_{i=1}^{N} k_{x_s,i}) \tag{4}$$

$$k_y = \frac{1}{N}(\Sigma_{i=1}^{N} k_{y_s,i}). \tag{5}$$

where $k_{x_s,i}$ and $k_{y_s,i}$ are the thermal conductivity of in-plane global thermal conductivity of a single ply. As for the out-of-plane thermal conductivity of a lamina, the serial model is applied.

$$k_z = N\left(\Sigma_{i=1}^{N} \frac{1}{k_{z_s}^i}\right)^{-1} \tag{6}$$

Table 1 – Thermal parameters of composite

Material	ρ (kg/m^3)	k (W/(m·K))	C_p (J/(m·K))
M40JB Carbon fiber	1.77	66.9/6.5	723
Epoxy resin	1.13	0.18	1200
UD-lamina	1.5588	44.93/1.68	837.1
[90,0,0,±27] Lamina	1.5588	18.4/1.68	837.1

3. Numerical Model

3.1 Anisotropic Thermal Conductivity of Composite

As shown in Fig.1, an angle, θ, generally exists between the local coordinate system coinciding with principal coordinate axes and the global coordinate system. A transformation process is needed to load anisotropic thermal conductivity to the CFRP. For the lamina cell, the principal coordinate axes, $x\prime$, $y\prime$ are parallel and perpendicular to the tangent of the airfoil, respectively. In a principal coordinate system, the thermal conductivity matrix is

$$\left[k'\right] = \begin{bmatrix} k_{x'} & 0 & 0 \\ 0 & k_{y'} & 0 \\ 0 & 0 & k_{z'} \end{bmatrix} \tag{7}$$

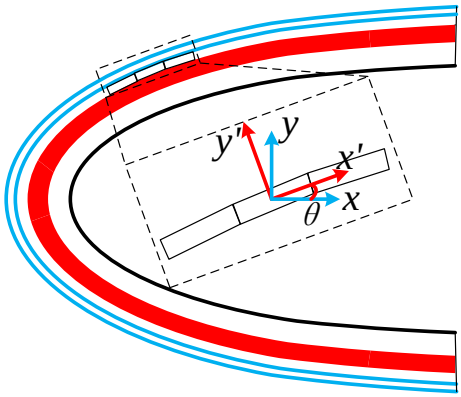

Figure 1 – The transformation relationship of the local coordinate system and the global coordinate system.

In a global coordinate system, the heat conduction equation in CFRP is

$$\rho C_p \frac{\partial T}{\partial t} = \nabla \cdot (k \nabla T) \tag{8}$$

The transformation matrix between the local coordinate system and the global coordinate system can be expressed as

$$[N] = \begin{bmatrix} l_1 & m_1 & n_1 \\ l_2 & m_2 & n_2 \\ l_3 & m_3 & n_3 \end{bmatrix} \tag{9}$$

where $l_i (i = 1,2,3)$ s the direction cosines of the principal axis x' with respect to the axes x, y and z. Similarly, the principal axis of m_i and $n_i (i = 1,2,3)$ are y' and z'. So, the thermal conductivity matrix in global coordinate is

$$[k] = \begin{bmatrix} k_{xx} & k_{xy} & k_{xz} \\ k_{yz} & k_{yy} & k_{yz} \\ k_{zx} & k_{zy} & k_{zz} \end{bmatrix} = [N]\left[k'\right][N]^T = \begin{bmatrix} l_1 & m_1 & n_1 \\ l_2 & m_2 & n_2 \\ l_3 & m_3 & n_3 \end{bmatrix} \begin{bmatrix} k_{x'} & 0 & 0 \\ 0 & k_{y'} & 0 \\ 0 & 0 & k_{z'} \end{bmatrix} \begin{bmatrix} l_1 & l_2 & l_3 \\ m_1 & m_2 & m_3 \\ n_1 & n_2 & n_3 \end{bmatrix} \tag{10}$$

Finally, the heat conduction equation in anisotropic CFRP composite is

$$\rho C_p \frac{\partial T}{\partial t} = \nabla \cdot \left([N] \left[k' \right] [N]^T \nabla T \right) \tag{11}$$

In present case, the transformation matrix, $[N]$ is

$$[N] = \begin{bmatrix} cos\theta & -sin\theta & 0 \\ sin\theta & cos\theta & 0 \\ 0 & 0 & 0 \end{bmatrix} \tag{12}$$

3.2 Anti-icing Model

Water impingement and local collection efficiency,β_{local}, is calculated by the Eulerian method as a one-way couple method because of the low volume fraction of the general supercooled droplet, which is appropriate [13]. The local collection is,

$$\beta_{local} = \frac{\alpha}{\alpha_\infty} \frac{\mathbf{u_d} \cdot \mathbf{n}}{\mathbf{u}_\infty} \tag{13}$$

There is no ice accretion on the surface for the present anti-icing condition. The mass and energy conservation of runback water is shown in Fig.2.

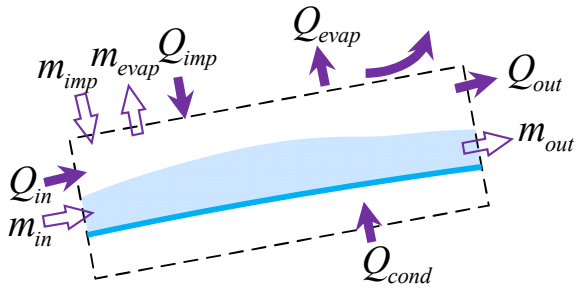

Figure 2 – Scheme of mass and energy analysis of a control volume.

The mass conservation equation of water film for current control volume is,

$$\dot{m}_{in} + \dot{m}_{imp} = \dot{m}_{out} + \dot{m}_{evap} \tag{14}$$

where $\dot{m}_{in}$ and $\dot{m}_{out}$ are the mass flux of runback water flowing into and out of the control volume, respectively. The impingement water mass flux is calculated by

$$\dot{m}_{imp} = \beta \cdot u_\infty \cdot \mathrm{LWC} \cdot dA \tag{15}$$

LWC is the liquid water content. dA is the area of current control volume. $\dot{m}_{evap}$ is the evaporation mass flux. According to Chilton-Colburn analogy, it can be obtained by

$$\dot{m}_{evap} = \frac{h_a A_c}{c_{p,a}} \left(\frac{Pr}{Sc} \right)^{2/3} \frac{M_d}{M_a} \cdot \left[\frac{p_{v,s}(T_w) - p_{v,e}}{p_e - p_{v,e}} \right] \tag{16}$$

h_a is the convection heat transfer efficiency. It is obtained by the Transition SST turbulence model with the constant wall temperature boundary condition in this paper.
The energy conservation equation is as follows,

$$\dot{Q}_{imp} + \dot{Q}_{in} + \dot{Q}_{cond} = \dot{Q}_{out} + \dot{Q}_{conv} + \dot{Q}_{evap} \tag{17}$$

where $\dot{Q}_{imp}$ is the total enthalpy of the impingement water entering the control volume. $\dot{Q}_{in}$ and $\dot{Q}_{out}$ are the total enthalpy of runback water flowing into and out of the control volume, respectively. $\dot{Q}_{cond}$ is

the heat flux through heat conduction provided by the heating element. And $\dot{Q}_{evap}$ is the total enthalpy of evaporated water. All of the terms can be expressed as the following equations,

$$\dot{Q}_{imp} = \dot{m}_{imp} \cdot \frac{{u_\infty}^2}{2} + \dot{m}_{imp} \cdot C_{p_d} \cdot T_\infty \tag{18}$$

$$\dot{Q}_{in} = \dot{m}_{in} \cdot C_{p_d} \cdot T_{w,in} \tag{19}$$

$$\dot{Q}_{out} = \dot{m}_{out} \cdot C_{p_d} \cdot T_w \tag{20}$$

$$\dot{Q}_{evap} = \dot{m}_{evap} \left(L_{evap} + T_w \cdot C_{p_d}\right) \tag{21}$$

$$\dot{Q}_{cond} = k \cdot \frac{\partial T}{\partial \mathbf{n}} \cdot A \tag{22}$$

where k is the thermal conductivity of the shield material. $\dot{Q}_{conv}$ is the convection heat flux, and it can be calculated by

$$\dot{Q}_{conv} = h_a \cdot (T_w - T_\infty) \cdot A \tag{23}$$

4. Results and Discussion

The anisotropic conductivity calculation method was validated by a cylindrical heat conduction equation in a semi-cylinder model. Besides, the experimental result and other numerical results are used to validate the present anti-icing model. The performances of anti-icing systems with a steel shield, anisotropic composite shield, and isotropic composite shield are evaluated by the developed anti-icing model. The thermal conductivities of three materials are shown in Tab.5.

4.1 Validation of Anisotropic Conductivity Calculation Method

A semi-cylinder model with cylindrical orthotropic thermal conductivity was used to validate the calculation method for anisotropic conductivity. In a cylindrical coordinate system, if the principal conductivities are along the r, Φ, and z axes, the steady heat conduction equation without heat source is,

$$k_r \frac{1}{r}\left(r\frac{\partial T}{\partial r}\right) + k_\Phi \frac{1}{r^2}\frac{\partial^2 T}{\partial \Phi^2} + k_z \frac{\partial^2 T}{\partial z^2} = 0 \tag{24}$$

As shown in Fig.3(a), the temperature distribution in semi-cylinder can be obtained according to Eq.24. Besides, the orthotropic thermal conductivity can also be calculated by the method presented in Sec3.1 The temperature distribution results is shown in Fig.3(b). Both results are almost identical. Therefore, the present calculation method for anisotropic thermal conductivity is applicable to the airfoil shape with a multi-layer structure.

Table 2 – Icing condition of 67A.

Parameters	Value
Far field pressure, $p_\infty(\mathrm{kPa})$	90
Inflow velocity, $u_\infty(\mathrm{m/s})$	89.4
MVD, $\mu\mathrm{m}$	20
LWC, $\mathrm{g/m^3}$	0.55
Inflow temperatrue, $T_\infty(^\circ\mathrm{C})$	-21.8
Attack angle, ($^\circ$)	0

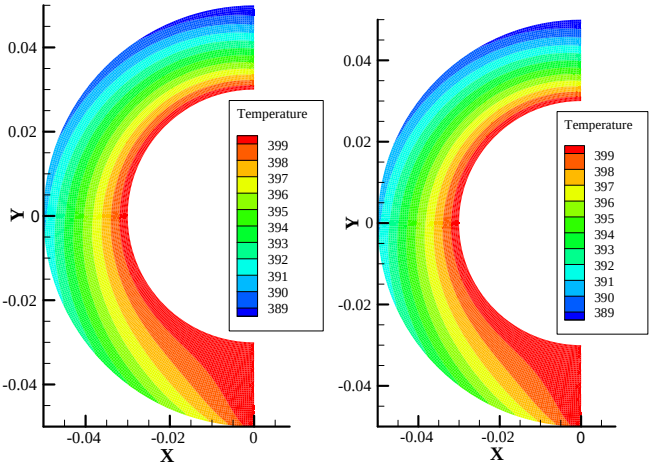

(a) Calculated in cylindrical coordinate (b) Calculated by present method

Figure 3 – Validation of coordinate transformation used to semi-cylinder with anisotropic conductivity.

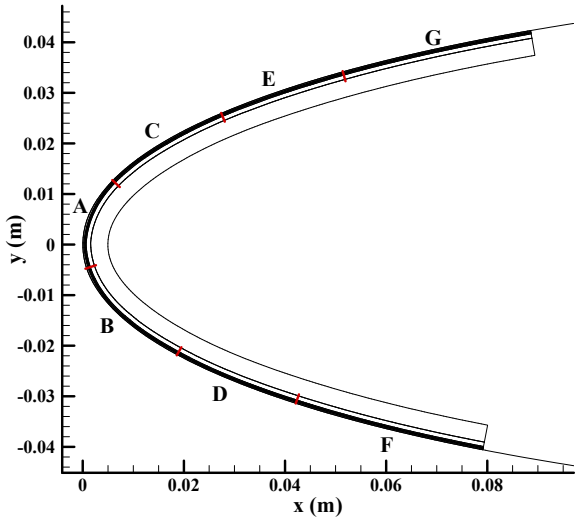

Figure 4 – The partition of the protection region.

Table 3 – Heat flux of each heating element.

Heating area	Heat flux ($\mathrm{kW/m^3}$)
F	20.15
D	21.70
B	32.55
A	43.40
C	26.35
E	18.60
G	18.60

4.2 Validation of Anti-icing Model

The case numbered 67A in Ref [10] was selected to validate the anti-icing model. It is an evaporative anti-icing mode in which the runback water ends almost at the end of the protection region. The icing condition of it is shown in Tab.2. The partition of heating areas is shown in Fig.4. There are seven heating elements embedded in the composite multi-layer structure. The heat fluxes of heating elements are listed in Tab.3. The closer the heating area is to the stagnation point, the higher the heat flux applied. The multi-layer structure of the electrothermal anti-icing system is shown in Fig.5. The thermal properties of the layers are listed in Tab.4. Composite can also be used as shield material for the anti-icing system. By replacing the shield material, the effect of the composite can be obtained.

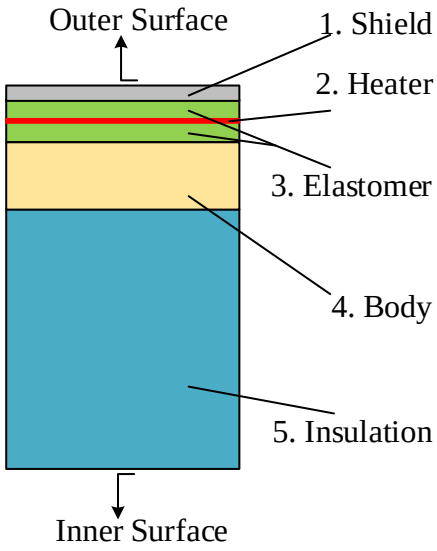

Figure 5 – The multi-layer structure of electrothermal anti-icing system.

Table 4 – Parameters of each layer.

Name	Thickness (mm)	ρ ($\mathrm{kg/m^3}$)	k ($\mathrm{W/(m\cdot K)}$)	C_p ($\mathrm{J/(m\cdot K)}$)
Shield	0.2	8025.25	16.3	502.416
Elastomer	0.28	1384	0.256	1256.04
Heating element	0.013	8906.26	41.0	385.186
Elastomer	0.28	1384	0.256	1256.04
Body	0.89	1794	0.294	1570.05
Insulation	3.43	648.75	0.121	1130.44

The local collection efficiency distribution obtained by the Eulerian method is shown in Fig.6. Fig.7

shows the comparison of temperature distribution on the anti-icing surface between the present anti-icing model and the methods used by other researchers[5, 7, 6]. In the middle region of the protection region, the present result shows a good agreement with the experiment. Besides, it is better than the result obtained by Bu[7]. The comparison of the runback water distribution is presented in Fig.6. The current mass flux of the runback water is similar to that of Bu and ANTICE. It indicates that the present anti-icing model can be used to evaluate the effect of the anisotropic thermal conductivity of composite in an electrothermal anti-icing system.

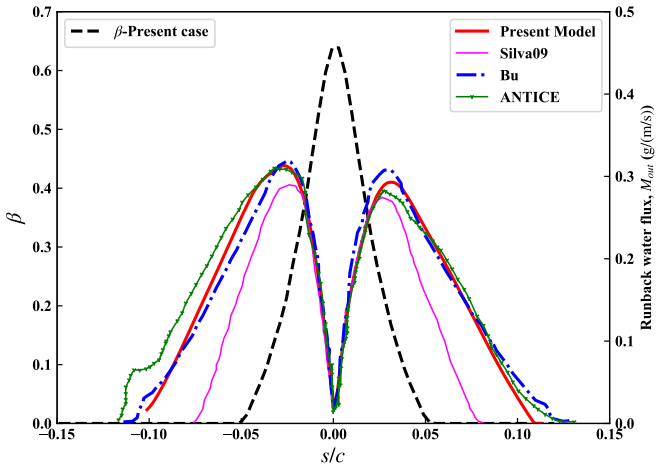

Figure 6 – The local water collection efficiency and mass flux of runback water.

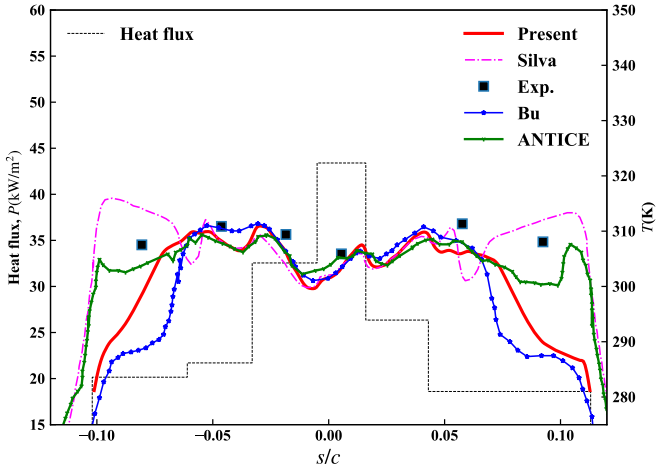

Figure 7 – Anti-icing surface temperature distribution compared with experimental and numerical results

Table 5 – Thermal conductivity of different shield materials.

Shield Material	k_1 $(\mathrm{W}/(\mathrm{m}\cdot\mathrm{K}))$	k_2 $(\mathrm{W}/(\mathrm{m}\cdot\mathrm{K}))$
Steel	16.3	16.3
Anisotropic composite	18.4	1.68
Isotropic composite	1.68	1.68

4.3 The Effect of Composite Shield on Electrothermal Anti-icing System

Fig.8 shows the temperature distributions on the anti-icing surface. Although the thermal conductivity of the three materials varies greatly, the difference in steady anti-icing surface temperature is small.

The surface temperatures are almost the same for the steel and isotropic composite shield. However, there are some small differences where the temperature changes drastically for the isotropic and anisotropic composite shield. This difference occurs mainly in a location with a large curvature close to the stagnation point. If the applied shield materials are isotropic, their thermal properties have little effect on the anti-icing surface temperature. However, the anisotropic thermal conductivity of the shield material will slightly reduce sharp changes in anti-icing surface temperature, especially in locations with large curvatures.

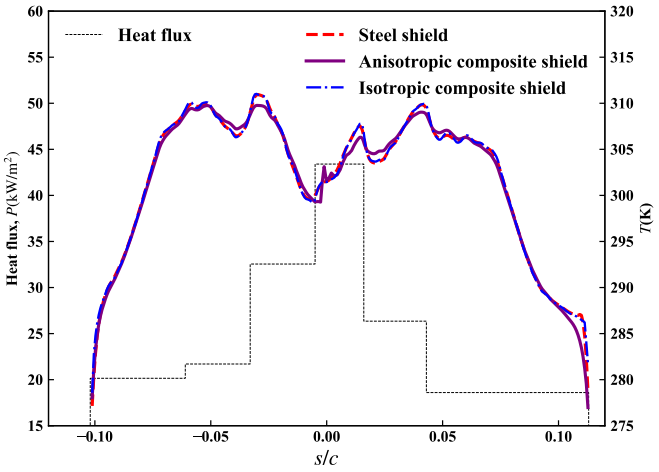

Figure 8 – Anti-icing surface temperature comparison of different shield materials.

The temperature distributions on the inner surface of the electrothermal anti-icing system for three shields are shown in Fig.9. Unlike the anti-surface temperature, there are significant differences between the three shield materials, mainly in large curvature locations. The inner temperature of the steel shield case is the lowest. Its thermal conductivity is the highest, facilitating heat transfer to the anti-icing surface. Moreover, the lowest thermal conductivity of the isotropic composite shield results in the highest inner surface temperature. The maximum difference between them can be 5K. However, it is apparent from Fig.9 that the temperature trend of steel shield and isotropic composite shield is the same. The maximum temperature is between the isotropic composite case and steel case for the anisotropic composite case. Its temperature trend is moderate at locations with great curvature. As shown in Fig.1, the thermal conductivity in the x' direction is larger than that in the y' direction. It facilitates heat flux distribution in the tangential direction, and the temperature trend becomes gentler than that of the isotropic composite shield case. The effect of the anisotropic thermal conductivity of composite on the inner surface temperature is significant.

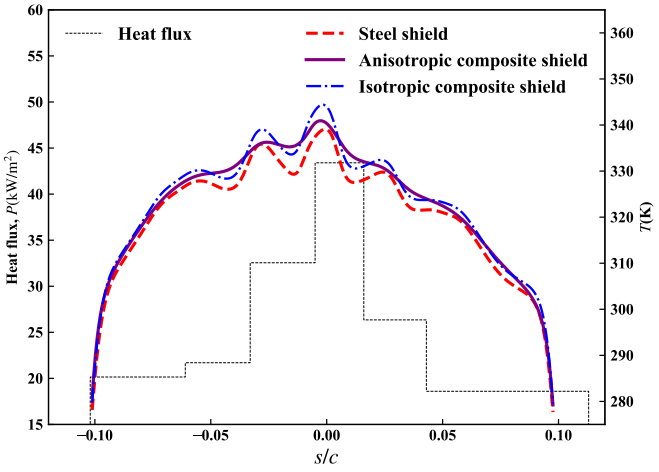

Figure 9 – Inner surface temperature comparison of different shield materials.

Fig.10 compares the mass fluxes of the runback water of three shield material cases. Due to the little difference in the anti-icing surface temperature, the runback water distributions are almost the same. The thermal conductivity of the shield materials has little effect on the runback water.

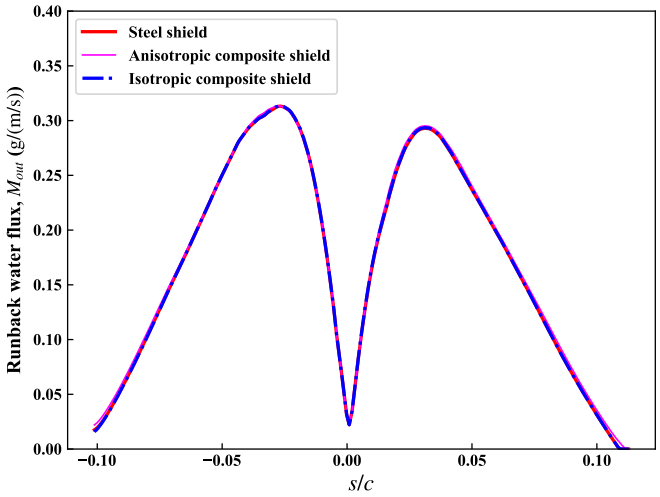

Figure 10 – Runback water distribution comparison of different shield materials.

The temperature distributions in the multi-layer structure of three cases are provided in Fig.11. The heat flux distribution in the heating element results in a significant temperature trend along the airfoil surface. The high-temperature region is concentrated near the stagnation point. The maximum temperatures in the multi-layer structure of steel shield case, anisotropic composite shield case, and isotropic composite shield are 342.64K, 343.83K, and 346.7K, respectively. The composite shield does not significantly increase the inner temperature of the electrothermal anti-icing system. However, the anisotropic thermal conductivity could result in a lower inner temperature. It is helpful to reduce the risk of high-temperature damage.

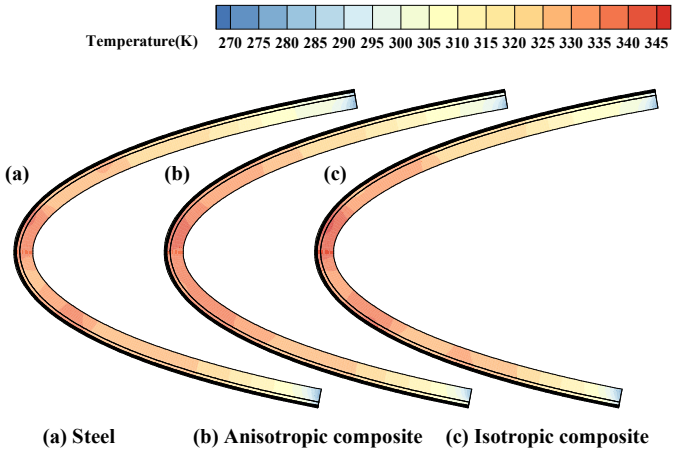

Figure 11 – Internal temperature distribution comparison of three shield materials

5. Conclusion

An anisotropic thermal conductivity calculation method is developed for composite materials. The validation of the anisotropic heat conduction model based on coordinate transformation is carried out by a semi-cylindrical model. The anti-icing model used in this paper is also validated using a NACA0012 model, and the results are compared with the previous experimental and numerical results. Coupling the anti-icing and anisotropic thermal conductivity models, we evaluate the electrothermal anti-icing system with a composite shield using a NACA0012 airfoil model. Moreover, the effects of shield material and the anisotropic thermal conductivity of composite on the temperature and runback water of

the anti-icing system are analyzed. The thermal properties of the shield materials have little effect on the temperature distribution and runback water distribution on the anti-icing surface. The anisotropic thermal conductivity of composite makes the temperature change gentler in the locations with large curvature. However, its effect is limited. The effect of anisotropic heat conduction on the inner surface temperature is significant. Due to the larger thermal conductivity of the tangential direction, the temperature changes gentler in the location with large curvature. Besides, the composite shield is not conducive to the heat transfer to the anti-icing surface. It can lead to a higher inner temperature compared with the steel shield.

Copyright Statement

References

[1] Electro-thermal ice protection system for the B-787. *Aircraft Engineering and Aerospace Technology*, Vol. 79, No. 6, 2007.

[2] Silva G, Silvares O and Zerbini E. Simulation of an Airfoil Electro-Thermal Anti-Ice System Operating in Running Wet Regime. *43rd AIAA Aerospace Sciences Meeting and Exhibit*, Reno, Nevada, 1374, 2001.

[3] Silva G, Silvares O and Zerbini E. Numerical simulation of airfoil thermal anti-ice operation. Part 1: Mathematical modeling. *Journal of Aircraft*, Vol. 44, No. 2, pp 627-633, 2007.

[4] Silva G, Silvares O and Zerbini E. Numerical simulation of airfoil thermal anti-ice operation. Part 2: Implementation and results. *Journal of Aircraft*, Vol. 44, No. 2, pp 624-641, 2007.

[5] Silva G, Silvares O and Zerbini E. Differential boundary-layer analysis and runback water flow model applied to flow around airfoils with thermal anti-ice. *1st AIAA Atmospheric and Space Environments Conference*, San Antonio, Texas, 3967, 2009.

[6] Wright, W, Al-Khalil, K, and Miller, D., Validation of NASA thermal ice protection computer codes. II-LEWICE/Thermal. *35th Aerospace Sciences Meeting and Exhibit*, Reno, Nevada, 50, 1997.

[7] Bu X, Lin G and Yu J. Numerical simulation of an airfoil electrothermal anti-icing system. *Proceedings of the Institution of Mechanical Engineers, Part G: Journal of Aerospace Engineering*, Vol. 227, No. 10, pp 1608-1622, 2012.

[8] Bu X, Lin G and Shen X. Numerical simulation of aircraft thermal anti-icing system based on a tight-coupling method. *International Journal of Heat and Mass Transfer*, Vol. 148, 119061, 2012.

[9] Shen X, Liu X and Lin G. Effects of anisotropic composite skin on electrothermal anti-icing system. *Proceedings of the Institution of Mechanical Engineers, Part G: Journal of Aerospace Engineering*, Vol. 233, No. 14, pp 5403-5413, 2019.

[10] Messinger B L. Equilibrium temperature of an unheated icing surface as a function of air speed. *Journal of the aeronautical sciences*, Vol. 20, No. 1, pp 29-42, 1953.

[11] Joven R, Das R and Ahmed A. Thermal properties of carbon fiber-epoxy composites with different fabric weaves. *SAMPE international symposium proceedings*, 14, 2012.

[12] Kulkarni M, Bardy R. A model of global thermal conductivity in laminated carbon/carbon composites. *Composites science and Technology*, Vol. 57, No. 1, pp277-285, 1997.

[13] Yang Q, Guo X and Dong W. Ice accretion and aerodynamic effects on a turbofan engine nacelle under takeoff conditions. *Aerospace Science and Technology*, Vol. 126, 107571, 2022.